

High frequency atmospheric gravity-wave properties using Fe-lidar and OH-imager observations

J. C. Diettrich,¹ G. J. Nott,¹ P. J. Espy,¹ G. R. Swenson,² X. Chu,² M. J. Taylor,³ D. M. Riggin,⁴ and D. C. Fritts⁴

Received 8 November 2004; revised 17 February 2005; accepted 23 March 2005; published 5 May 2005.

[1] Simultaneous iron resonance lidar density profiles, OH intensity images and MF-radar wind measurements have been used to determine the horizontal and vertical components of high-frequency ($\ll \sim 1$ hour) atmospheric gravity waves (AGW). Previous investigations predicted that AGW information from lidars and imagers could only be combined over a limited range. Here, a novel approach to increasing the utility of the simultaneous lidar and OH imager measurement are presented. By temporally high-pass filtering each altitude-bin of the lidar profiles, the vertical wavelengths of AGW typically observed with the OH imager become apparent. Measured OH imager horizontal wavelengths were converted into vertical wavelengths using the dispersion relationship and background winds, showing that the instruments were able to observe the same waves. Hence, the lidar-imager combination is able to access the intrinsic wave components to allow investigation of AGW propagation and an assessment of the chemical waves effects on minor species chemistry. **Citation:** Diettrich, J. C., G. J. Nott, P. J. Espy, G. R. Swenson, X. Chu, M. J. Taylor, D. M. Riggin, and D. C. Fritts (2005), High frequency atmospheric gravity-wave properties using Fe-lidar and OH-imager observations, *Geophys. Res. Lett.*, *32*, L09801, doi:10.1029/2004GL021944.

1. Introduction

[2] The dynamics and thermal balance of the mesosphere are influenced by atmospheric gravity waves (AGW) [Fritts and Alexander, 2003]. Vincent [1984] showed that a significant part of the energy of AGW is transported into the mesosphere by waves with periods less than 1 hour that are characterized by horizontal wavelengths < 150 km and vertical wavelengths between 20 and 10 km. Energy fluxes measured for waves with periods of 2.5–5 and 0.5–1.25 hours were 11.4×10^4 and $36.1 \times 10^4 \text{ Wm}^{-2}$, respectively. Due to their vertical extent being larger than the typical ~ 8 km thickness of emitting airglow layers, the horizontal wavelengths, velocities and periods of these waves have been readily observed with all-sky airglow imagers [Swenson and Mende, 1994; Taylor *et al.*, 1995]. However, to obtain the intrinsic properties of an AGW from this

information, either the vertical component of the wave or the background wind is required. Lidars resonant with atoms or molecules present at an airglow height range, e.g. Fe, could supply this vertical AGW information. However, lidars, with their high vertical resolution, typically observe the short vertical wavelength waves [Gardner and Taylor, 1998]. Hence, the two instruments have previously not been combined to give a complete horizontal and vertical picture of propagating gravity waves. We present here co-coordinated Fe resonance lidar, airglow imaging and radar-wind observations of propagating gravity waves. We show that by temporally high-pass filtering the lidar profiles, it is possible to observe the vertical structure of the same waves imaged by the airglow camera. Combining these results allows the complete three-dimensional properties of these AGW, and hence their intrinsic properties, to be obtained.

2. Instruments

2.1. Fe-Lidar

[3] As part of the collaboration between the University of Illinois and the British Antarctic Survey (BAS), a Fe-Boltzmann temperature lidar has been deployed at Rothera. This resonant lidar system, capable of daytime and nighttime observations, operates at 372 and 374 nm to probe two manifolds of the ground state of the mesospheric Fe [Chu *et al.*, 2002]. In this way, vertical profiles of Fe density and temperature at altitudes between ≈ 78 and 100 km could be obtained, although only the Fe density derived from the 372 nm, ground-state channel, will be discussed here. Individual photon count profiles were integrated for 2.5 minutes, and the system was gated to obtain a 48 m height resolution. For the measurements presented here, the 2.5 min profiles were smoothed using a Hamming window width of approximately a third of the observed period, with the observations periods ranging from 38–100 minutes. The sequence of Fe density profiles from the lidar was used to determine both the vertical wavelength and period of AGWs passing through the Fe layer.

2.2. OH Imager

[4] In collaboration with Utah State University, BAS operates an all-sky airglow imager less than 200 m from the lidar site. The imager, with 512×512 pixel CCD array and fisheye lens, records nighttime airglow activity near the mesopause (see Espy *et al.* [2004] for more details on the system). Images of the hydroxyl (OH) emission layer from the atmospheric height of 88 km, with a full width at half maximum (FWHM) thickness of ~ 8 km, were integrated for 15 seconds on the CCD array and repeated every 120 seconds, as images of other airglow layers were also recorded.

¹British Antarctic Survey, Cambridge, UK.

²Department of Electrical and Computer Engineering, University of Illinois, Urbana, Illinois, USA.

³Space Dynamics Laboratory and Department of Physics, Utah State University, Logan, Utah, USA.

⁴Colorado Research Associates, Boulder, Colorado, USA.

Table 1. Summary of Results From the OH Imager, MF Radar and Fe Lidar, Including Calculated Intrinsic Period (τ_{int}) and Wave Amplitude (A) as Observed With the Fe Lidar^a

Time [UT]/Date	OH-Imager			MF Radar		Calculated		Fe-Lidar		
	τ_{obs} (min)	λ_{H} (km)	Az[°]	\bar{U}_z [m/s]	\bar{U}_m [m/s]	τ_{int} (min)	λ_{V} (km)	λ_{V} (km)	τ_{obs} (min)	A[%]
0420–0600 30-Apr-2003	64	134.7	242	6.8(4.2)	11.2(4.1)	61	12.5(2.0)	10.8	65	12
0846–0933 22-Jul-2003	20	40.5	250	18.3(6.7)	−1.5(3.6)	40	7.2(3.1)	7.5	22	3.2
1004–1042 22-Jul-2003	30	58	232	6.1(6.6)	6.9(4.7)	29	14.4(2.5)	12.8	29	9

^aThe uncertainties are shown in parentheses.

Prior to analysis the images were centred on zenith, rotated to align the cardinal directions, and then flat-fielded. Finally, the stars were removed using the technique described by *Tang et al.* [2003]. Resulting images had a field of view (FOV) of 150 km \times 150 km, and the horizontal wavelengths, directions of propagation and periods of AGW passing through the OH layer could be determined.

2.3. MF Radar

[5] In order to compare the vertical and horizontal wave properties from the lidar and imager and verify that the same waves were observed, the background horizontal winds were required for the dispersion relationship. These were provided by an MF-radar operating at Rothera as part of a co-operation between BAS and the US National Science Foundation [*Jarvis et al.*, 1999]. The radar operates at a frequency of 1.98 MHz by detecting partial reflection scatter from weak ionization in the mesosphere with spatially separated antennae. The full correlation analysis technique [*Briggs*, 1984; *Vincent and Lesicar*, 1991] was used to derive estimates of the zonal and meridional components of the horizontal wind. Between 75 and 100 km, where most of the scatter occurs, the winds were sampled every 120 s with an altitude resolution of 4 km.

3. Analysis and Results

[6] Data time periods for investigation were selected based on overlap of lidar, OH imager and MF-radar data, and the presence of quasi-monochromatic AGW. This led to three periods of interest for which the wave properties were derived. These time periods, along with the derived quantities, are listed in Table 1.

[7] As an example, Figure 1 shows the zenith pixel intensity from the OH imager for the first time period between 0420 to 0600 UT on 30 April 2003. An initial estimate showed an AGW to be present with a period \sim 65 min. In order to identify a coincident wave in the lidar data, each Fe density profile was weighted with a model OH volume emission rate profile [*Swenson and Gardner*, 1998] and integrated. The resulting time series, which shows small gaps due to lidar maintenance, is also shown in Figure 1, and the presence of the same AGW present in the imager data is evident.

[8] Retrieving the vertical wave component from the Fe density profiles was achieved by applying a high-pass filter to the Fe density profiles. For each altitude bin, the consecutive profiles were high-pass filtered in the time domain, resulting in Fe-perturbation density profiles. Here, for the first period under investigation, a filter passing all periods $<$ 90 minutes was used. The resulting Fe-perturbation density profiles are given in Figure 2. For presentation

purposes only, the perturbed profiles were hamming window smoothed in time and altitude domains with FWHM of 15 min and 1000 m, respectively. A clear wave structure through the Fe density profiles is visible.

[9] The vertical wavelength was determined using the Lomb-Scargle method. The vertical power spectral density of each Fe-perturbation profile was taken, and then averaged over the time interval. The dominant oscillation in the resulting power spectral density had a vertical wavelength of 10.8 km.

[10] The OH images were used to retrieve horizontal wavelength, direction of propagation and period of the AGW. To determine the dominant wave passing through the OH imager's field-of-view, images spaced \approx 120 sec apart were differenced to enhance the \sim 65 min wave [*Swenson and Mende*, 1994]. The 2-D wavenumber spectrum was calculated for each difference image, and averaged over the sequence of all image differences over the first time period. Figure 3 shows the resulting spectrum. The most dominant wave had a horizontal wavelength λ_{H} of 134.7 km and an azimuth of 242° (WSW).

[11] In order to determine the wave period, a band-pass filter in the wavenumber domain was constructed to isolate the dominant wave with a FWHM bandwidth of $4.2 \times 10^{-4} \text{ m}^{-1}$ and centred at the wavenumber of the most dominant wave, $46.6 \times 10^{-6} \text{ m}^{-1}$. This band-pass filter was applied to the wavenumber spectra of each individual image, leading to smoothed OH images. The intensity of the OH along the smoothed image in the propagation direction was taken. By concatenating those slices of consecutive images as described by *Swenson et al.* [2003], the traveling speed of the AGW can be refined. Using this technique an observed period, T_0 , of 64 min was determined, giving an observed phase speed, $C_0 = \lambda_{\text{H}}/T_0$, of 35 m/s.

[12] To fully establish that the lidar and imager were observing the same AGW, the horizontal OH imager wave-

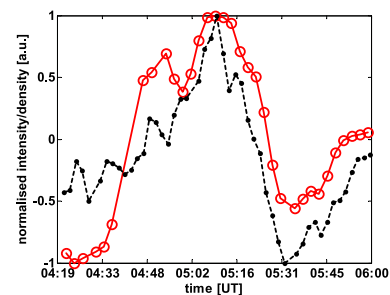


Figure 1. Weighted and normalized lidar density and OH intensity of 30 April 2003. Normalized Fe density is presented by open circles (o), and normalized OH intensity is given by the dashed dotted line (— · — · —).

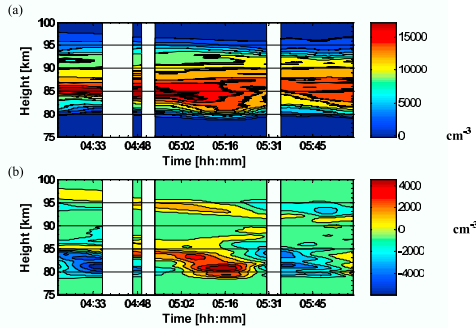


Figure 2. Fe density profile (a) and Fe density perturbation (b) of 30 April 2003 from 0420 to 0600 UT. The white bars represent missing data. The iron density profiles were hamming window smoothed for presentation purposes only.

length was converted into its corresponding vertical wavelength using the dispersion relationship. The following atmospheric conditions were assumed; incompressibility and wave periods of about an hour or shorter, for which the dispersion relationship is given by:

$$m^2 = \frac{N^2 - \omega^2}{\omega^2 - f^2} k^2 - \frac{1}{4H^2}. \quad (1)$$

Here, $m = 2\pi/\lambda_V$ and $k = 2\pi/\lambda_H$ are the vertical and horizontal wavenumbers, respectively, f is the inertial frequency, N is the Brunt-Väisälä (buoyancy) frequency and H is the scale height. The buoyancy frequency was calculated using an average temperature profile measured with Fe lidar, and calculated for the OH layer height and width. The intrinsic frequency is given by $\omega = 2\pi|C_0 - \bar{U}|/\lambda_H$, with C_0 the observed phase speed. The background wind speed, \bar{U} , was measured with the MF radar.

[13] The mean wind averaged over the model OH layer was found to be 6.8 ± 4.2 m/s in the zonal, and 11.2 ± 4.1 m/s in the meridional components. The mean wind speed was calculated by fitting a mean value and a sinusoidal wave to the wind speed data. The period of the sinusoidal wave was set equal to the period of the investigated AGW (64 min). The uncertainty of the mean wind speed is then given by the standard deviation of the fit to the data in respect to the mean value. Using equation (1), the measured OH imager horizontal wavelength yields a vertical wavelength of 12.5 km (± 2.0 km) in good agreement with the vertical wavelength observed by the lidar.

[14] Two further periods were analyzed using the same technique. The first period extended from 0846 to 0933 UT on 22 July 2003, and the second from 1004 to 1042 UT on the same day. A summary of the measured wave parameters and those calculated from the dispersion relationship for the three time periods is given in Table 1. The dominant oscillation in the 0846 to 0933 UT filtered lidar data had a period of ≈ 22 min and a measured vertical wavelength of 7.5 km. The OH imager measured an observed period of 20 min and a horizontal wavelength of 40.5 km, giving an observed phase velocity of 34 m/s at an azimuth of 250° . The derived vertical wavelength of 7.2 km (± 3.1 km) using equation (1) is in good agreement with the vertical

wavelength measured with the lidar. Similar good agreement is found for the data section between 1004 and 1042 UT on the same day. The lidar measured a dominant wave period of 29 min with vertical wavelength of 12.8 km. The OH imager measured an observed period of 30 min and a horizontal wavelength of 58 km with direction of 232° . This converted to a vertical wavelength of 14.4 km (± 2.5 km). Here again, good agreement has been found between the vertical wavelengths measured with the lidar and calculated from the OH imager.

4. Conclusion

[15] Atmospheric gravity waves with periods of one hour or shorter, observed with imagers, carry a large portion of energy. Here we have shown that by means of temporally high-pass filtering each altitude bin of the lidar density data, one can retrieve the vertical properties of the same AGW observed with the OH imager.

[16] This technique applied to Fe-lidar data presented here gave intrinsic vertical wavelengths between 7 and 13 km for observed periods between 20 minutes and 1 hour. Simultaneous OH Imager measurements revealed similar periods with horizontal wavelengths between 40 and 135 km. To demonstrate that the lidar and imager were observing the same AGW, mean winds derived from coincident MF radar were used to derive intrinsic vertical wavelengths from the OH imager using the dispersion relationship.

[17] Using this analysis technique, the lidar and imager observations can give a complete picture of the horizontal and vertical properties of an AGW, demonstrating that the wave is freely propagating. It also shows that the intrinsic parameters of the wave can be ascertained using only these two instruments. The portable nature of airglow imagers will therefore broaden the possibility to perform investigations where such intrinsic parameters are required. Such studies include observations of energy flux, wave-induced changes in minor-species concentrations, and AGW propagation studies.

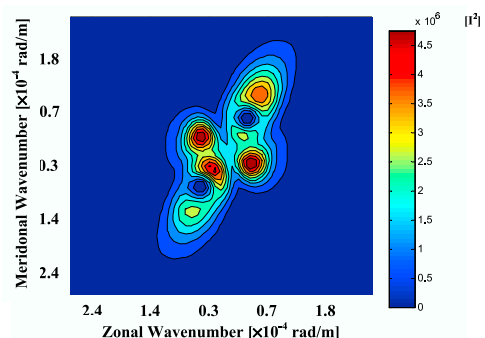


Figure 3. Summed FFT image difference for 30 April 2003 for time period of 0420 to 0600 UT. The most dominant wave had a horizontal wavelength of 134.7 km and a direction of 242° . 2-dimensional FFT spectrum was rearranged, so that smallest frequencies for each dimension were located in center of picture, for optical presentation purposes only, and given in units of OH-imager intensity squared.

[18] **Acknowledgments.** The operation of all instruments at Rothera station is supported by the UK Natural Environment Research Council. In addition, the lidar was supported by US National Science Foundation (NSF) grants ATM-03-034357; the airglow imager by NSF grants ATM-0003180 and OPP-9816465; and the MF radar by NSF grants OPP-9319068 and OPP-9813629.

References

- Briggs, B. H. (1984), The analysis of spaced sensor records by correlation techniques, in *Handbook for MAP*, vol. 13, edited by R. A. Vincent, pp. 166–186, Sci. Comm. on Sol. Terr. Phys. Sec., Univ. of Ill., Urbana.
- Chu, X., W. Pan, G. C. Papen, C. S. Gardner, and J. A. Gelbwachs (2002), Fe Boltzmann temperature lidar: Design, error analysis, and initial results at the North and South Poles, *Appl. Opt.*, *41*(21), 4400–4410.
- Espy, P. J., G. O. L. Jones, G. R. Swenson, J. Tang, and M. J. Taylor (2004), Tidal modulation of the gravity-wave momentum flux in the Antarctic mesosphere, *Geophys. Res. Lett.*, *31*, L11111, doi:10.1029/2004GL019624.
- Fritts, D. C., and M. J. Alexander (2003), Gravity wave dynamics and effects in the middle atmosphere, *Rev. Geophys.*, *41*(1), 1003, doi:10.1029/2001RG000106.
- Gardner, C. S., and M. J. Taylor (1998), Observational limits for lidar, radar and airglow imager measurements of gravity wave parameters, *J. Geophys. Res.*, *103*, 6427–6437.
- Jarvis, M. J., G. O. L. Jones, and B. Jenkins (1999), New initiatives in observing the Antarctic mesosphere, *Adv. Space Res.*, *24*, 611–619.
- Swenson, G. R., and C. S. Gardner (1998), Analytical models for the responses of the mesospheric OH* and Na layers to atmospheric gravity waves, *J. Geophys. Res.*, *103*, 6271–6294.
- Swenson, G. R., and S. B. Mende (1994), OH emissions and gravity waves (including a breaking wave) in all-sky imagery from Bear Lake, Utah, *Geophys. Res. Lett.*, *21*, 2239–2242.
- Swenson, G. R., A. Liu, F. Li, and J. Tang (2003), High frequency atmospheric gravity wave damping in the mesosphere, *Adv. Space Res.*, *32*, 785–793.
- Tang, J. F., L. G. Kamalabadi, L. G. Rumsey, and G. R. Swenson (2003), Point source suppression for atmospheric wave extraction from airglow imaging measurements, *IEEE Trans. Geosci. Remote Sens.*, *42*, 146–152.
- Taylor, M. J., M. B. Bishop, and V. Taylor (1995), All-sky measurements of short period waves imaged in the OI (557.7 nm), Na (589.2 nm) and near infrared OH and O₂ (0,1) nightglow emission during the ALOHA-93 campaign, *Geophys. Res. Lett.*, *22*, 2833–2836.
- Vincent, R. A. (1984), Gravity-wave motions in the mesosphere, *J. Atmos. Terr. Phys.*, *46*, 119–128.
- Vincent, R. A., and D. Lesicar (1991), Dynamics of the equatorial mesosphere: First results with a new generation partial reflection radar, *Geophys. Res. Lett.*, *18*, 825–828.

X. Chu and G. R. Swenson, Department of Electrical and Computer Engineering, University of Illinois, 1308 West Main Street, Urbana, IL 61801, USA.

J. C. Diettrich, P. J. Espy, and G. J. Nott, British Antarctic Survey, High Cross, Madingley Road, Cambridge CB3 0ET, UK. (jadi@bas.ac.uk)

D. C. Fritts and D. M. Riggan, Colorado Research Associates, 3380 Mitchell Lane, Boulder, CO 80301, USA.

M. J. Taylor, Space Dynamics Laboratory and Department of Physics, Utah State University, Logan, UT 84322-4145, USA.